The Astrophysical Journal Supplement Series, 194:24 (11pp), 2011 June doi:10.1088/0067-0049/194/2/24

A DUAL-BAND MILLIMETER-WAVE KINETIC INDUCTANCE CAMERA FOR THE IRAM 30 m TELESCOPE

A. Monfardini[1], A. Benoit[1], A. Bideaud[1], L. Swenson[1,10], A. Cruciani[1,11], P. Camus[1], C. Hoffmann[1], F. X. Désert[2], S. Doyle[3], P. Ade[3], P. Mauskopf[3], C. Tucker[3], M. Roesch[4], S. Leclercq[4], K. F. Schuster[4], A. Endo[5], A. Baryshev[6], J. J. A. Baselmans[6], L. Ferrari[6], S. J. C Yates[6], O. Bourrion[7], J. Macias-Perez[7], C. Vescovi[7], M. Calvo[8], and C. Giordano[9]
[1] Institut Néel, CNRS & Université Joseph Fourier (UJF), Grenoble F-38042, France; monfardini@grenoble.cnrs.fr
[2] Institut de Planétologie et d'Astrophysique, UJF & CNRS-INSU, Grenoble F-38041, France
[3] Cardiff School of Physics and Astronomy, Cardiff University, Cardiff CF24 3AA, UK
[4] Institut de RadioAstronomie Millimétrique (IRAM), Saint Martin d'Hères F-38406, France
[5] Kavli Institute of NanoScience, Delft University of Technology, 2628 CJ Delft, The Netherlands
[6] SRON, Netherlands Institute for Space Research, 3584 CA Utrecht and 9700 AV Groningen, The Netherlands
[7] Laboratoire de Physique Subatomique et de Cosmologie, UJF & CNRS/IN2P3 & INPG, F-38026 Grenoble, France
[8] Dipartimento di Fisica, Universitá di Roma La Sapienza, I-00185 Roma, Italy
[9] Fondazione Bruno Kessler, I-38123 Povo (TN), Italy
Received 2011 February 8; accepted 2011 March 21; published 2011 May 6

ABSTRACT

The Néel IRAM KIDs Array (NIKA) is a fully integrated measurement system based on kinetic inductance detectors (KIDs) currently being developed for millimeter wave astronomy. The instrument includes dual-band optics allowing simultaneous imaging at 150 GHz and 220 GHz. The imaging sensors consist of two spatially separated arrays of KIDs. The first array, mounted on the 150 GHz branch, is composed of 144 lumped-element KIDs. The second array (220 GHz) consists of 256 antenna-coupled KIDs. Each of the arrays is sensitive to a single polarization; the band splitting is achieved by using a grid polarizer. The optics and sensors are mounted in a custom dilution cryostat, with an operating temperature of ∼70 mK. Electronic readout is realized using frequency multiplexing and a transmission line geometry consisting of a coaxial cable connected in series with the sensor array and a low-noise 4 K amplifier. The dual-band NIKA was successfully tested in 2010 October at the Institute for Millimetric Radio Astronomy (IRAM) 30 m telescope at Pico Veleta, Spain, performing in-line with laboratory predictions. An optical NEP was then calculated to be around 2×10^{-16} W Hz$^{-1/2}$ (at 1 Hz) while under a background loading of approximately 4 pW pixel^{-1}. This improvement in comparison with a preliminary run (2009) verifies that NIKA is approaching the target sensitivity for photon-noise limited ground-based detectors. Taking advantage of the larger arrays and increased sensitivity, a number of scientifically relevant faint and extended objects were then imaged including the Galactic Center SgrB2 (FIR1), the radio galaxy Cygnus A, and the NGC1068 Seyfert galaxy. These targets were all observed simultaneously in the 150 GHz and 220 GHz atmospheric windows.

Key words: instrumentation: detectors – radio continuum: galaxies – radio continuum: general – submillimeter: galaxies – submillimeter: general – techniques: miscellaneous

Online-only material: color figures

1. INTRODUCTION

The importance of millimeter and submillimeter astronomy is now well established. In particular, three main areas of millimeter continuum research have motivated the rapid development of new technologies:

1. The study of star-forming regions in the Galaxy (Ward-Thompson et al. 2007). The pre-stellar phases in molecular clouds are hidden by cold dust (around 10 K) which can only be observed at submillimeter wavelengths.
2. The investigation of high-redshift galaxies (Lagache et al. 2005). The redshift effect at submillimeter wavelengths counteracts the distance dimming (Blain et al. 2002).
3. The measurement of cosmic microwave background (CMB) temperature anisotropies (either primordial or secondary). At a temperature of 2.725 K, the CMB spectrum peaks at millimeter wavelengths. Of particular interest is the Sunyaev–Zel'dovich effect (Birkinshaw 1999), which distorts the CMB spectrum at millimeter and radio wavelengths and can be used to map the distribution of hot gas in clusters of galaxies.

Throughout the previous decade, instruments utilizing hundreds of individual bolometers in focal plane arrays have dominated continuum submillimeter and millimeter astronomy (e.g., MAMBO2, BOLOCAM). Full-sampling arrays with up to thousands of pixels in a single array are now reaching maturity, offering increased mapping speed and decreased per-pixel manufacturing costs (e.g., Apex-SZ, SPT, SCUBA2, LABOCA). Despite these considerable advances, further array scaling is strongly limited by the multiplexing factor of the readout electronics.

A promising alternative to traditional bolometers is the kinetic inductance detector (KID). First demonstrated less than 10 years ago (Day et al. 2003), a KID consists of a high-quality superconducting resonant circuit electromagnetically coupled to a transmission line.

In a superconductor, the conduction electrons are condensed into charge-carrying Cooper pairs. At DC it is well known that these Cooper pairs do not undergo scattering and hence do not contribute any electrical impedance. However at non-zero frequencies energy can be stored, and later returned to the

[10] Current address: California Institute of Technology, 367-17 Pasadena, CA 91125, USA.
[11] Also at Dipartimento di Fisica, Universitá di Roma La Sapienza, I-00185 Roma, Italy.

electromagnetic fields, in the inertia of the Cooper pairs. This results in an effective reactive impedance known as the kinetic inductance. In contrast, the kinetic inductance is not significant in normal metals. In that case, the very short carrier scattering time results in dissipation of the inertial energy through Joule heating. Mediated by lattice vibrations superconductivity also results in an energy gap in the carrier density of states. Incident photons with an energy exceeding the gap energy can break a Cooper pair, producing two quasiparticles and a concurrent change in the complex surface impedance $\sigma(\omega) = \sigma_1(\omega) - j\sigma_2(\omega)$, where $\sigma_2(\omega)$ is directly related to the kinetic inductance. The result is a shift in the KID resonance frequency and a change of the resonator quality factor. Both can be read out by the measurement electronics. The non-local Mattis–Bardeen theory can be used to solve for changes in both $\sigma_1(\omega)$ and $\sigma_2(\omega)$ due to incident radiation, allowing a direct calculation of the resonator frequency response to illumination (Gao 2008).

Typically, a KID is designed to resonate from 1 to 10 GHz and exhibits a loaded quality factor exceeding $Q_L > 10^5$. Thus, each KID occupies a bandwidth of order $\Delta f = f/Q_L \sim$10–100 kHz. A single KID only loads the transmission line within Δf around its resonant frequency. The KID resonant frequency can easily be controlled geometrically during the circuit design. It is therefore possible to couple a large number of KIDs to a single transmission line without interference as long as the inter-resonance frequency spacing exceeds $2\Delta f$. The inter-resonance frequency spacing and the total bandwidth of the measurement electronics set a limit on the total number of pixels which can be simultaneously read out on a single measurement line (Mazin 2004). Current frequency-multiplexing measurement electronics are limited to at most a few hundred pixels per measurement cable. This is expected to grow into the thousands of pixels per cable within the next decade, vastly improving the multiplexing factor in comparison with existing array technologies.

In order to absorb incident radiation, it is necessary to impedance match the KID to free space at the target wavelength. Currently, there are two methods for meeting this criterion. The first is to use a geometry known as the lumped-element KID (LEKID) which separates the resonator into an inductive meander section and a capacitor. At the target wavelength, the inductive meander approximates a solid absorber. By accounting for the resonator and substrate impedances and the cavity formed with the sample holder, it is possible to directly impedance match the LEKID to free space (Doyle et al. 2009). Alternatively, a lens and antenna structure can be used to adapt the resonator to free space. Due to the increased geometric complexity, it has proven more difficult to achieve satisfactory device performance with antenna structures than with direct absorption LEKIDs. Despite this drawback, antenna-coupled KIDs remain a very active area of research due to their frequency selectivity (Schlaerth et al. 2008).

For both LEKIDs and antenna-coupled KIDs, detection is achieved in the same manner, described above, once the incident radiation has been absorbed.

We are currently developing a fully integrated measurement system based on KIDs known as the Néel IRAM KIDs Array (NIKA). The two primary goals of NIKA are to assess the viability of KIDs for terrestrial astronomy and to develop a filled-array, dual-band resident instrument for the Institute for Millimetric Radio Astronomy (IRAM) 30 m telescope at Pico Veleta, Spain. Based on a custom-designed dilution cryostat with a base temperature of ∼70 mK (Benoit et al. 2008), a first generation single-band NIKA prototype was previously tested at the Pico Veleta telescope in 2009 October (Monfardini et al. 2010). This successful measurement was the first to directly compare the performance of LEKID and antenna-coupled KID designs.

Leveraging the experience gained from the first generation NIKA, an improved instrument has been designed and tested at the IRAM 30 m telescope in 2010 October. This second generation system includes a large number of enhancements. Dual-band optics, integrating a polarization-sensitive splitter and a new baffling structure, allow simultaneous imaging at 150 GHz and 220 GHz. Resonator design modifications resulted in improved single-pixel sensitivity. Faster digital-signal-processing electronics enable synchronous measurement of up to 112 pixels for each measurement band. Fabrication of a sky simulator to replicate typical measurement conditions at the telescope facilitated improved array testing and quality control. Along with a detailed discussion of these system upgrades, we present here the results of the 2010 October measurement campaign. This includes a discussion of the limiting noise sources, an analysis of the system performance determined using calibration sources such as planets, and an estimate of the improved full-system sensitivity. Finally, we present astronomically relevant observations of a number of faint and extended sources in both measurement bands which were previously unattainable with the less sensitive first generation NIKA.

2. THE DUAL-BAND OPTICS

The new dual-band NIKA is engineered to fit the receiver cabin of the IRAM telescope in Pico Veleta, Spain. The 30 m primary mirror (M1) and the hyperbolic secondary (M2, $D =$ 2 m) are installed directly on a large alt-azimuth mounting. The incident beam is directed into the receiver cabin through a hole in M1 using a standard Cassegrain configuration. A rotating tertiary (M3) provides a fixed focal plane (Nasmyth focus). The optical axis, in order to conform to the dimensions of the cabin, is deviated by two flat mirrors (M4 and M5). M4 can rotate between two fixed positions, selecting either heterodyne or continuum instruments.

NIKA re-images the large telescope focal plane onto the small sensitive area covered by the KIDs. The demagnification factor is around 6.6, achieving a well-adapted scale of 5 arcsec mm^{-1} on the detector plane. This is accomplished using two flat mirrors (M6, M7), one bi-conical mirror (M8), and three high-density polyethylene (HDPE) corrugated lenses (L1, L2, L3). The lens corrugation consists of machined concentric grooves, providing a soft transition between vacuum ($n = 1$) and HDPE ($n = 1.56$) to reduce reflective losses. The size of the grooves is 0.4 mm × 0.4 mm in depth and width, while the width of the ridges is 0.4 mm. L1 is located at room temperature and coincides with the cryostat vacuum isolation window. L2 is mounted on the screen at 4 K, while the final L3 lenses (one per array) are installed at the coldest stage just in front of the arrays (∼70 mK). A simple grid polarizer with a grid pitch of 4 μm was inserted at 45° with respect to the main optical axis before the final L3 lenses. Since all KID designs currently employed in NIKA are sensitive to a single polarization, this is an efficient way to realize beam splitting for the two frequency bands. A schematic of the optical design is presented in Figure 1.

For both arrays, the lenses are telecentric. That is, each point of the detector plane is illuminated with the same aperture with the chief ray perpendicular to the surface. This strongly

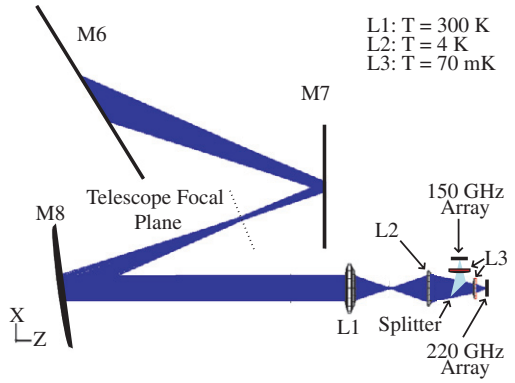

Figure 1. NIKA optical design. Two flat mirrors (M6, M7) orient the beam on the bi-conic mirror M8. The rays enter the cryostat through the window, coincident with lens L1. A grid polarizer located at 70 mK between lenses L2 and L3 splits the beam and redirects the radiation to two polarization-sensitive arrays, the first optimized for 150 GHz and the second for 220 GHz. The band-defining filters centered at 150 GHz and 225 GHz are mounted directly on the flat face of each L3 lens.

(A color version of this figure is available in the online journal.)

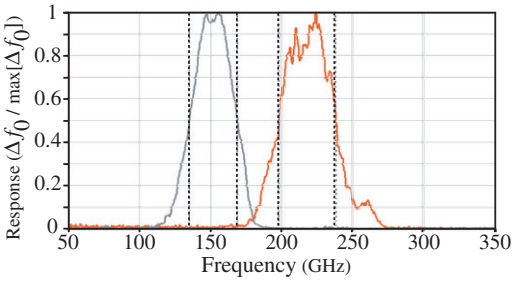

Figure 2. Normalized spectral response of the NIKA detectors. The 3 dB measured bandwidths are 135–169 GHz and 198–238 GHz.

(A color version of this figure is available in the online journal.)

reduces potential systematic errors related to overlap of the incident beam with the intrinsic pixel lobe. The detector plane is oversampled with respect to the diffraction spot size: the full width at half-maximum is about 3 mm for the 150 GHz band and 2 mm for the 220 GHz band. The pixel pitches are 2.25 mm and 1.6 mm, for final aperture ratios of $0.75F\lambda$ and $0.80F\lambda$, respectively. The useful, projected field of view is approximately 1.6×1.6 arcmin^2 for the 150 GHz array and 1×1 arcmin^2 for the 220 GHz array.

A series of filters and baffling are used to reject unwanted radiation. To reduce off-axis radiation, a multi-stage, black-coated baffle is installed at 4 K between L1 and L2. This is further augmented with a cold pupil at 70 mK. Three infrared-blocking filters are mounted on the first two radiative screens held at a temperature of ∼150 K and ∼70 K by cold helium vapors. Three additional low-pass filters are installed on the 4 K and 1 K screens. The radiation entering the 70 mK stage is thus restricted to frequencies $\nu < 300$ GHz. The final band definition is achieved using a series combination of a high-pass and a low-pass filter behind the final lens L3, just in front of the detector array. The spectral response of NIKA was characterized using a Martin–Puplett interferometer (Durand 2007). The results, displayed in Figure 2, exhibit good agreement with the atmospheric transparency windows and coincide with the expected response based on the individual filter cutoff frequencies. Taking into consideration the tabulated HDPE transmission and the individual filter specifications, we estimate a total optical transmission coefficient of ≈0.4 for the NIKA optics.

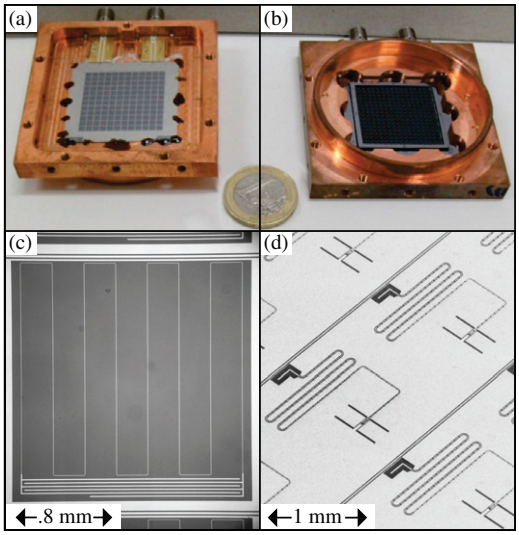

Figure 3. Mounted arrays and pixel micrographs: (a) 144 pixels LEKIDs array and (b) 256 pixels antenna-coupled array. KID micrographs: (c) LEKID and (d) antenna-coupled KID. For both micrographs, light regions indicate where metal is present and dark areas where the substrate dielectric is exposed.

(A color version of this figure is available in the online journal.)

3. THE DETECTORS AND READOUT ELECTRONICS

The second generation NIKA implements a 144 pixel array of LEKIDs for 150 GHz detection and a 256 pixel array of antenna-coupled KIDs for 220 GHz sensing. An image of the mounted arrays is shown, along with micrographs of the individual pixels, in Figure 3.

For the LEKIDs array, fabrication commenced with an argon plasma surface treatment of a 300 μm thick high-resistivity silicon wafer (>5 kΩ cm^{-1}). Next, a 20 nm aluminum film was deposited via DC sputtering. The final array structure was subsequently defined with UV lithography followed by wet etching.

For the antenna-coupled KIDs, a hybrid material structure necessitated a more complex fabrication strategy. The basic KID consists of a quarter-wave coplanar waveguide (CPW) resonator. One end of the resonator is coupled to the measurement transmission line while the other end is grounded. A twin-slot antenna focuses incident radiation on the grounded end. Half the length of the resonator center strip, on the grounded end, is made of aluminum; the rest of the center strip on the coupler side, and the entire ground plane, is made of NbTiN. Fabrication consisted of a 300 nm thick sputter deposition of NbTiN (Barends et al. 2010) on an HF-passivated high-resistivity silicon wafer (>10 kΩ cm^{-1}). A 100 nm aluminum film was then sputter deposited through a lift-off mask into the plasma-etched slots in the ground plane to complete the resonator center strip. Aluminum air bridges were then used to connect the ground planes of the CPW in order to suppress microwave mode conversion, reduce the cross talk, and improve the beam pattern. The radiation is concentrated and focused on the antennas by silicon elliptical lens segments of 1.6 mm diameter, arranged in a rectangular grid of 1.6 mm spacing. This lens array is glued on the back side of the KID sample. The misalignment between the lens and the twin-slot antenna is less than 10 μm, ensuring good coupling efficiency.

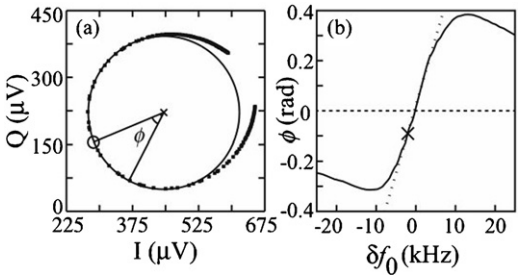

Figure 4. KID calibration. (a) *I*–*Q* frequency scan across a resonance. Complex phase is calculated by fitting each resonance to a circle (shown); the phase angle is then determined with respect to the center of the resonance circle as indicated by the × . The minimum transmission is marked with a small circle. (b) Frequency shift vs. complex phase. The x on the curve indicates the maximum frequency shift when Mars transits the pixel.

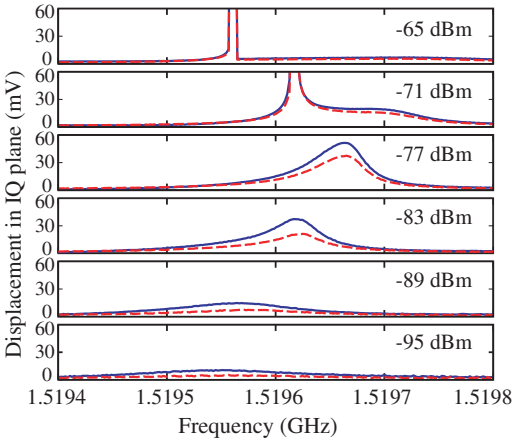

Figure 5. Readout power and frequency optimization. The velocity magnitude $[(\Delta I/\Delta f)^2 + (\Delta Q/\Delta f)^2]^{1/2}$ (solid, blue) is plotted along with the optical response $[(\Delta I/\Delta T)^2 + (\Delta Q/\Delta T)^2]^{1/2}$ (dashed, red) for each point around a resonance. The velocity was measured while making linear frequency steps $\Delta f = 6$ kHz around the resonance. The optical response was measured by sweeping the resonance in frequency with a cold focal plane ($T \sim 70$) K and then at increased temperature $\Delta T = 7$ K.

(A color version of this figure is available in the online journal.)

The general principles of frequency-multiplexed KID readout have been described in detail elsewhere (Swenson et al. 2009; Yates et al. 2009; Monfardini et al. 2010). The current digital electronics used for the NIKA readout were developed in the context of an international collaboration known as the open source readout (OSR; Duan et al. 2010). This system was based on a digital platform known as ROACH, itself having been developed in the context of another collaboration known as Center for Astronomy Signal Processing and Electronics Research (Parsons et al. 2006). The ROACH hardware provides powerful signal processing capabilities by integrating a field-programmable gate array, an on-board power pc, and a variety of high-speed communication interfaces. Building on this, the OSR developed new high-speed, dual-input analog-to-digital and dual-output digital-to-analog interface cards. For NIKA, both of these cards were clocked by the same rubidium-referenced external clock generator. Operating at 466 megasamples s^{-1}, the resulting useful intermediate-frequency (IF) measurement bandwidth of the NIKA readout was 233 MHz. In order to drive the individual pixels and subsequently read out their state, the NIKA Collaboration developed customized software to use with the OSR hardware. Similar to standard lock-in techniques, the implemented algorithm allowed 112 separate measurement tones to be generated and simultaneously monitored within the IF measurement bandwidth.

The NIKA readout uses a standard up–down converter configuration based on two IQ mixers per board to transpose the generated IF frequency comb to the resonator operating frequencies. One ROACH board and a set of IQ mixers were used for each array. Currently, the LEKID array operates in the frequency range 1.27–1.45 GHz. Within this bandwidth, 104 pixels and 8 off-resonance blind tones could be used for measurement. The antenna-coupled KID array has a central pixel core operating at 5–5.2 GHz. Due to the larger inter-resonator frequency spacing of this array, only 72 core pixels could be simultaneously measured out of the total 256 pixels in the array.

The response of every pixel in an array is measured simultaneously and broadcast via UDP packets by the ROACH electronics to the control computers at a rate of 22 Hz. The individual pixel responses are composed of a pair of in-phase (I) and quadrature (Q) values which result from the final stage of digital mixing and low-pass filtering. These values can be translated into the traditional transmission phase and amplitude using the identities $\theta = \arctan(Q/I)$ and amplitude$^2 = I^2 + Q^2$. An alternative approach is to plot these values in the complex plane. An example of a standard frequency sweep around a resonance is provided in Figure 4(a). Small changes in illumination result primarily in motion around this curve and thus it is convenient to define a new angle ϕ about the center of curvature (I_c, Q_c):

$$\phi = \arctan\left(\frac{Q - Q_c}{I - I_c}\right) - \phi_0, \quad (1)$$

where ϕ_0 rotates the plane such that the curve intersects the x-axis at the resonance frequency f_0.

We have observed that the KID response to radiation depends critically on the driving power and frequency of the readout electronics. While still not fully understood, it is reasonable to conjecture that this dependence could be caused by nonlinear thin film effects, quasiparticle generation or suppression in the superconductor, or a field-dependent dielectric behavior. A plot of the velocity around the resonance curve for a linear frequency sweep and the measured response to a change in the focal plane temperature is shown in Figure 5 for increasing readout powers. For low readout power (<90 dBm), the responsivity of the KID is weak. As the power is increased, the KID responsivity and the velocity are seen to increase and to shift to higher frequencies. Beyond a critical readout power, a discontinuity in the resonance emerges and the frequency shift changes directions and moves back toward lower frequencies. While the greatest responsivity is obtained in this region, the region near the discontinuity is unstable and not currently well understood. For the current measurement a readout power of ∼−77 dBm, just below the appearance of the discontinuity, was used. For the frequency selection, it is also important to note that while the maxima in responsivity and velocity coincide, these generally do not occur near an extremum of the traditional S_{21} amplitude or phase or their corresponding derivatives. The exact relationship between the responsivity and the shape of the S_{21} curve is observed to depend on a number of implementation details, including pixel cross-talk and impedance loading of the transmission line. For this reason, the NIKA software now implements a calculation of the velocity around the resonance during calibration.

For low intensity radiation, the density of photo-generated quasiparticles in a KID is proportional to the incident photon flux. To first order, this results in a linear shift in the kinetic inductance and, for thin films, a subsequent linear shift in the

resonance frequency (Swenson et al. 2010). That is

$$\delta f_0 = -C f_0^3 \delta L_K \propto -\frac{f_0^3}{n_s^2}\delta P_i, \quad (2)$$

where C is a constant, n_s is the Cooper pair density, and δP_i is the incident power. A plot of the phase ϕ versus the frequency shift from resonance δf_0 for a typical KID is shown in Figure 4(b) along with the maximum frequency shift during a transit of Mars. From this plot it is clear that $\partial\phi/\partial f$ is approximately linear for relevant astronomical signals. Thus, $\phi \propto \delta P_i$ with the constant of proportionality being determined during a calibration scan. One caveat is that under large background changes, which can result from weather changes or telescope repointing, n_s changes substantially and causes a significant shift in f_0. For this reason, an automatic procedure was implemented to properly determine (I_c, Q_c) and ϕ_0 before every scan taken on the telescope to assure that the measurement would remain in the dynamic range of the KIDs. This recalibration is currently achieved in under 60 s.

4. THE SKY SIMULATOR

In order to replicate real observing conditions and to properly estimate the amount of stray light on the detectors, we have built a testing tool to complement MP interferometer measurements and classical chopper tests alternating between hot and cold sources. Simply called the sky simulator, the basic idea consists in cooling down a large, black disk with the same dimensions as the telescope focal plane. This cold disk simulates the background temperature in ordinary ground-based observing conditions. On a telescope the main contributions to the background are the atmospheric residual opacity, which is weather dependent, and the emissivities of the mirrors. The typical background temperature of the IRAM Pico Veleta telescope is in the range 30–100 K. For the sky simulator, the cooling of the background disk is achieved by using a single-stage pulse-tube refrigerator. A large window in the sky simulator cryostat is fabricated in 4 cm thick HDPE which is sufficiently transparent at millimeter wavelengths. The minimum background temperature that can be achieved is 50 K, limited by the radiation absorbed by the large, black, cold disk. An image of the sky simulator can be seen in Figure 6.

To simulate an astronomical source, a high-emissivity ball with a diameter of 5–10 mm was placed in front of the sky simulator window at room temperature. The ball is mounted on a motorized XY stage enabling movement with respect to the fixed disk. The angular speed on the sky of a typical on-the-fly scan at the IRAM telescope is 10 arcsec s^{-1}. Accounting for the ∼300 m effective focal length of M1 and M2, this corresponds to a scan speed of 15 mm s^{-1} on the telescope focal plane. This velocity is well within the capabilities of the XY translator. A comparison of two single-pixel transits, the first taken with the telescope and the second with the sky simulator, is shown in Figure 6(c).

The sky simulator temperature can be adjusted continuously between 50 K and 300 K, allowing an accurate estimation of the detector response and a direct determination of the noise equivalent temperature (NET). To perform this measurement, the spectral noise density $S_n(f)$, expressed in Hz Hz$^{-1/2}$, is calculated at a fixed background temperature. The background temperature is then increased by δT and the shift in the KID resonance frequency is measured. This yields the KID frequency response R expressed in Hz K^{-1}. The NET is then given by

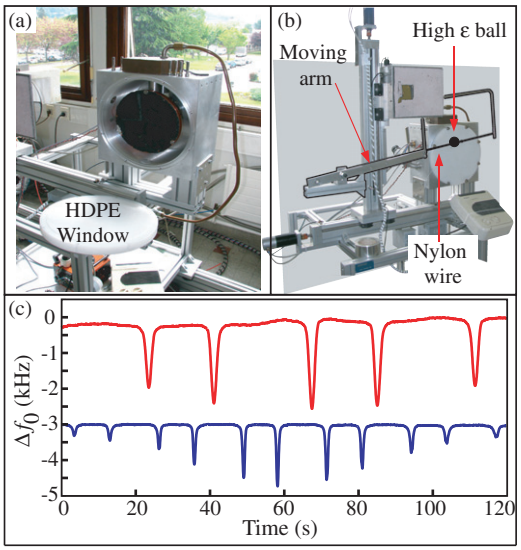

Figure 6. Sky simulator. (a) HDPE cryostat window removed. The cold disk simulating the sky background is shown; its diameter is 24 cm. (b) Fully assembled system. The translation arm, nylon wire, and high emissivity ball are outlined for visibility. The ball moves at a controlled rate in front of the HDPE window, faking a real source on the sky. In particular, on-the-fly telescope scans are easily simulated (Bideaud 2010). (c) Sky simulator validation. A real on-the-fly scan of Uranus taken at the 30 m telescope is shown (red, upper) along with a laboratory on-the-fly scan using the sky simulator (blue, lower). The telescope angular scan speed was 10 arcsec s^{-1}. The linear scan speed of the sky simulator was 30 mm s^{-1}, corresponding to a telescope angular speed of 20 arcsec s^{-1}. For both traces, the transit of the source was observed with a single pixel.

(A color version of this figure is available in the online journal.)

$$\mathrm{NET}(f) = \frac{S_f(f)}{R}. \quad (3)$$

Laboratory tests performed on the LEKID array indicated an average NET per pixel of 4 mK Hz$^{-1/2}$ at a standard representative frequency of 1 Hz. Accounting for the optical chain transmission and including a 50% reduction due to the polarizer, this corresponds to an optical noise equivalent power (NEP) of approximately 2×10^{-16} W Hz$^{-1/2}$. The best single-pixel LEKIDs have an optical NEP, under realistic 4–8 pW loading per pixel, around 6×10^{-17} W Hz$^{-1/2}$. These results indicate that no conceptual limitations exist for using KIDs in the next generation large arrays of ground-based millimeter-wave instruments.

The sky simulator has also been used to estimate the amount of undesired stray light incident on the detector arrays. This measurement required two steps. First, the pixel frequency shifts were recorded, while the sky simulator was moved in the optical axis direction from its customary position at the telescope focal plane up to the cryostat window. Next, the sky simulator was returned to the telescope focal plane and the background temperature was then increased until an equivalent frequency shift was affected. This resulted in an estimated stray-light temperature of ∼35 K which corresponds to ∼4 pW of parasitic power per pixel at 150 GHz. The unwanted radiation has thus been reduced by more than a factor of two compared with the first generation NIKA and is now comparable to the best sky conditions at Pico Veleta.

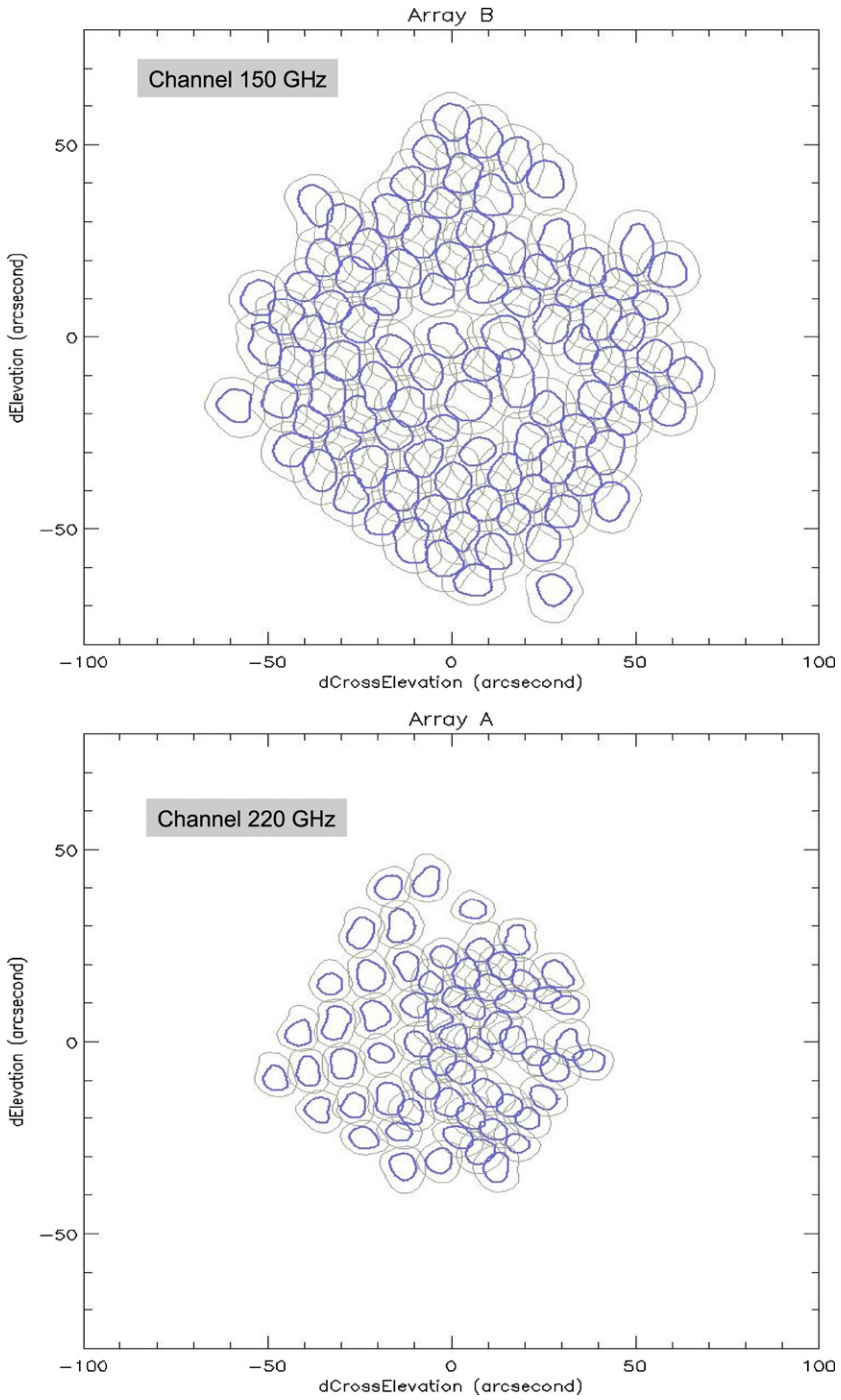

Figure 7. 80% (blue, thin) and 50% (gray, thick) contours of the beams as measured on Mars on the 2010 October 20. Top: 2 mm array (98 valid KID), bottom: 1.4 mm array (62 valid KID).

(A color version of this figure is available in the online journal.)

5. RESULTS

The dual-band NIKA run took place in 2010 October. The instrument was installed in the receiver cabin of the IRAM 30 m telescope at Pico Veleta, Spain, and operated remotely from the control room. The cool-down of the instrument was also performed remotely, taking approximately 18 hr to reach the operating temperature of 70 mK.

Astronomical data from the two arrays are reduced offline with dedicated software. The raw data (I,Q) are converted to complex phase angle using the closest previous KID calibration. Then a conversion to an equivalent frequency shift is done with the same calibration using the derivative of the frequency with the complex phase at the zero phase, as described in Figure 4. Data are thus internally converted to frequencies which are assumed to be linear with the absorbed photon counts, as in Equation (2). After opacity correction, and using Mars as the primary calibrator, we obtain that the overall median gain is of 14 mJy beam^{-1} Hz^{-1} and 9 mJy beam^{-1} Hz^{-1} for the 1.4 and 2 mm (220 GHz and 150 GHz) channels, with a 30% dispersion. The focal plane geometry of each array is measured by using scanning maps of planets (see Figure 7).

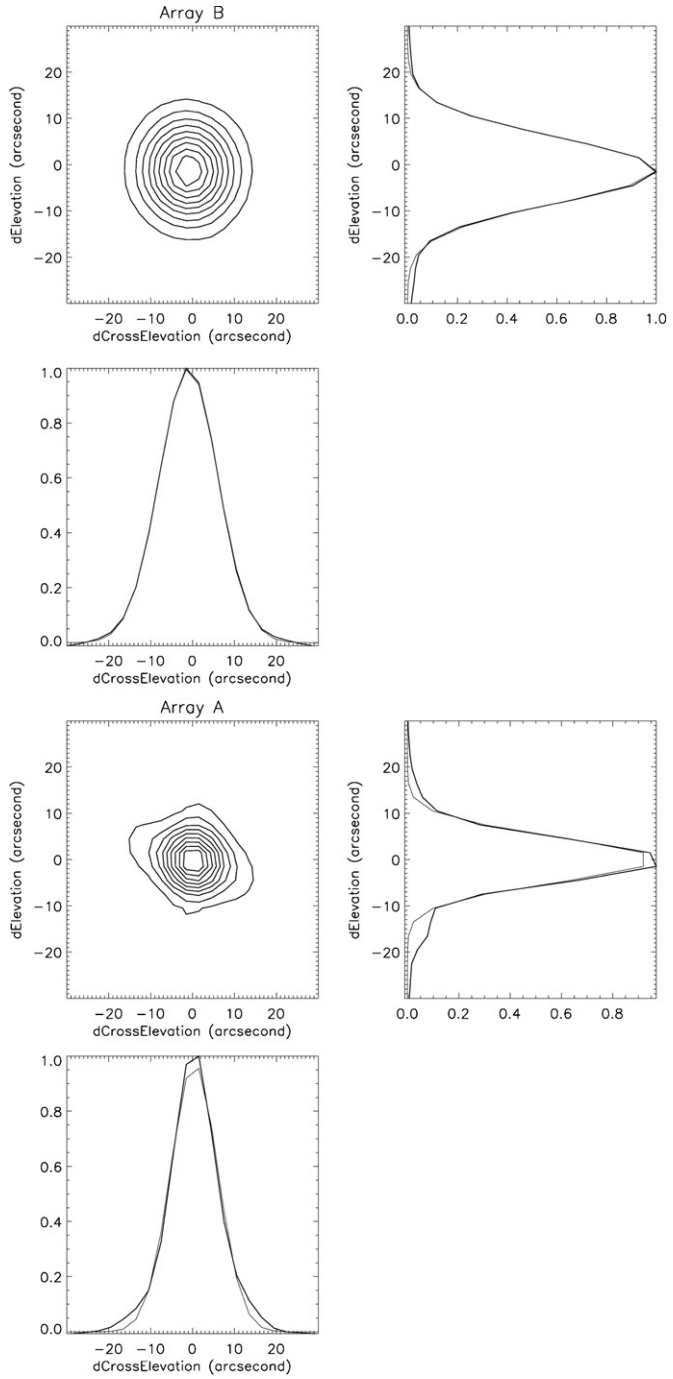

Figure 8. Beam contours obtained on Mars with levels at 10%–90%. Azimuth and elevation slices along the center are shown on the sides along with the slice of a two-dimensional Gaussian fit. The FWHM is 16.7 (resp. 12.4) arcsec at 2 mm (resp. 1.4 mm).

The fitted focal plane geometry is found by matching the pixel position in the array as measured on the wafer to the measured position on planets, by optimizing a simple set of parameters: a center, a tilt angle, and a scaling expressed in arcsec mm^{-1}. Most detectors are within less than 2 arcsec of their expected position. The beam width is also found from planet measurements. Typically the FWHM is 12.4 and 16.7 arcsec for the two arrays (1.4 and 2 mm, respectively, see Figure 8) with a dispersion of 1 arcsec. This is close to the diffraction limit for the 2 mm array. Pixelization effects have not been removed from this estimate. This might explain why the 1.4 mm beam is larger by 20% than the diffraction size.

We were able to observe many types of objects. We here show only examples of the results that are currently analyzed. Usually, the observing scan mode is a simple on-the-fly mapping, composed of constant-elevation sub-scans, with the telescope sweeping in azimuth back and forth. The detector data are processed in the time domain (calibration and filtering) before being projected on a common map, using the focal plane geometry as described above. The noise is evaluated at the detector level by histogram Gaussian fitting outside the sources. The noise is then propagated to the map level. The final map is obtained by co-adding the individual detector maps with an inverse square noise weighting scheme. From known sources and reproducibility from scan to scan and from detector to detector, the photometric accuracy is estimated to be 30%. New methods are being investigated to improve this photometric offline processing accuracy.

We present SrgB2(FIR1) as an example of extended source, Cygnus A as an example of a multiple source, and NGC1068 as an example of weak source with a new 2 mm flux measurement.

Figure 9 shows a dual map of the Galactic Center obtained in 900 s of integration time. This complex region reveals at least three compact sources. The very center has a flux of 76 ± 3Jy and 17.7 ± 0.7Jy at 1.4 and 2 mm, respectively.

In Figure 10, we show Cygnus A (3C405), a well-known radio source with two prominent radio lobes. The maps were obtained with two scans making a total integration time of 2200 s. The central source flux is of 0.76 ± 0.09 Jy (resp. 0.89 ± 0.04 Jy) at 1.4 mm (resp. 2 mm). The flux errors are dominated by photometric noise and not detector noise. The two radio lobes (named AB and DE) have a flux (taken at the positions given by Wright & Birkinshaw 2004) of 1.63 ± 0.09 Jy and 1.65 ± 0.08 Jy at 1.4 mm. At 2 mm, the measured fluxes are 2.47 ± 0.13 Jy and 2.36 ± 0.10 Jy. The 1.4 mm fluxes can be compared with BIMA 1.3 mm interferometer observations by Wright & Birkinshaw (2004). The BIMA fluxes of the nucleus, and the AB and DE radio lobes are 0.48, 0.54, and 0.97 Jy, respectively. The spectral dependence ($F_\nu \propto \nu^{-1}$) as measured by Wright & Birkinshaw (2004) is recovered on the two radio lobes with the NIKA camera. Nevertheless, the NIKA fluxes are a factor 1.70 higher. We think that this is an angular resolution effect. For example, using the 1.1 mm flux measured by Eales et al. (1989) with a 19 arcsec beam and applying the above spectral dependence, we expect 0.74, 1.1, and 1.5 Jy at 1.4 mm for the flux of the nucleus and the two radio lobes which is in agreement with what we obtain.

Figure 11 shows a secure detection of NGC1068, a nearby galaxy with an active galactic nucleus. The map is obtained with five scans and a total integration time of 1260 s. Its flux is 142 ± 25 mJy at 1.4 mm and 66 ± 3 mJy at 2 mm. This is the central flux measured with a Gaussian of 12 and 19 arcsec, respectively. For this map, a sky noise decorrelation has been used, which is based on a linear regression with the detector signals when off-source. The northeast–southwest extension at 1 mm is larger but aligned with interferometric IRAM Plateau de Bure Interferometer (PdBI) observations (Krips et al. 2006). The PdBI measured flux for the core and the jet is 28 ± 2 mJy at 231 GHz. This is smaller than the NIKA flux measurement which is more consistent with the flux of 170 ± 30 mJy measured by Thronson et al. (1987), indicating the presence of a diffuse extended component. This component is expected (Hildebrand et al. 1977), based on consideration of the far-infrared spectral

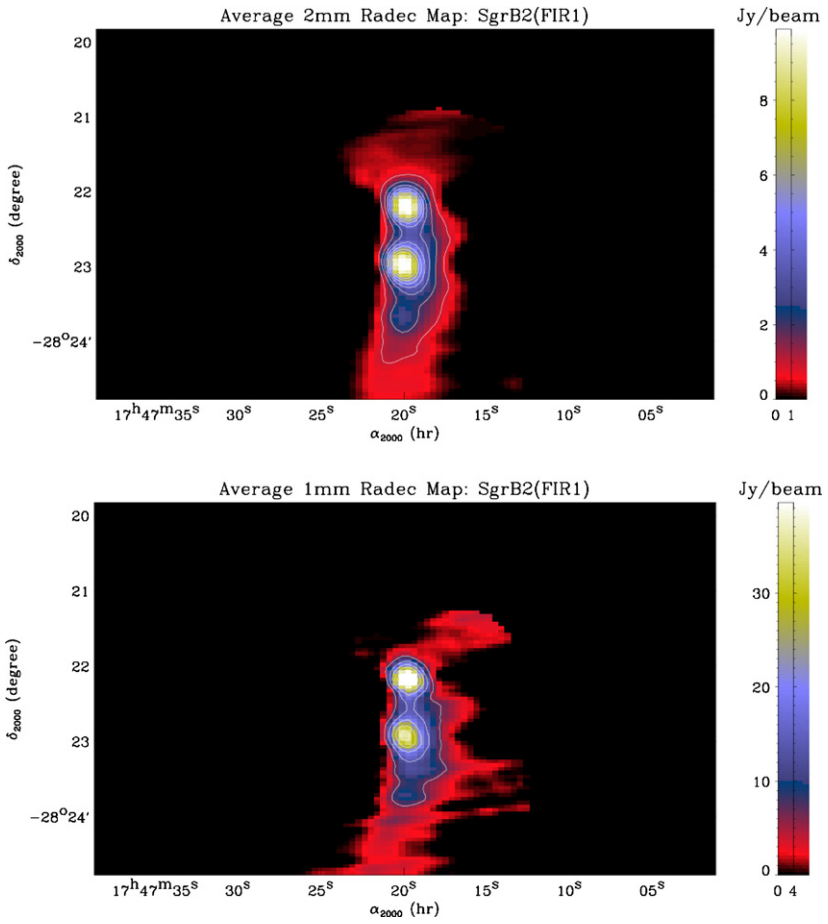

Figure 9. SgrB2(FIR1) maps at both frequencies. The Galactic Center map is complex and shows at least three common sources and one north–south extended component that does not coincide in the two maps.

(A color version of this figure is available in the online journal.)

energy distribution. It is likely to come from heated dust in the circumnuclear region.

From deep integration on weak sources and using sky noise decorrelation, we are able to derive the effective sensitivity of the camera, in the present early state of data reduction and sky noise subtraction techniques. We obtain a weak-source flux detectivity of 450 and 37mJy $s^{1/2}$ at 1.4 and 2 mm, respectively. The 1.4 mm detectivity is satisfactory for an initial 1.4 mm KID prototype. The 2 mm detectivity shows a major improvement by a factor three with the best value obtained in the 2009 NIKA run (Monfardini et al. 2010). This detectivity is almost at the level of the state-of-the-art APEX-SZ TES detectors (Schwan et al. 2010) albeit obtained here with a larger telescope. An NET of 6 m K $s^{1/2}$ is deduced from this value. A sensitivity to the SZ effect can be obtained as 3×10^{-5} $hr^{1/2}$ in the y Compton parameter for one beam, although this may be complicated by the SZ extension. SZ measurements will be reported in a later publication.

The individual detector performances were determined using noise spectra taken while on-telescope following the same strategy implemented with the sky simulator. A typical noise spectrum, taken with the LEKID array during a standard on-the-fly scan, is shown in Figure 12. The data are fit using a sum of two power laws:

$$N_f(f) = Af^{\alpha} + Bf^{\beta}. \quad (4)$$

The low-frequency fluctuations seen while observing are due to the expected source and sky noise ($\alpha = -1.35$), while the higher frequency fluctuations can be attributed to the detector noise ($\beta = -0.15$). The detectors' noise is relatively flat, in contrast with previous measurements where an $N_{\theta,f} \propto f^{-0.5}$ dependence was observed (Monfardini et al. 2010; Gao et al. 2007). This seems to indicate a substantial reduction, at least in the case of the LEKID array, of the intrinsic frequency noise due to random variations of the effective dielectric constant. For the 220 GHz (1.4 mm) antenna-coupled KID array, the spectral slope does not contradict the cited model and exhibits the expected $f^{-0.5}$ dependence. We recognize however that dark measurements would be more suited to draw definitive conclusions concerning fundamental noise properties of the resonators.

Using the frequency response of Mars, a primary calibrator, and the noise spectra, we calculate a raw detector sensitivity of the order of 25 mJy $Hz^{-1/2}$ for the LEKID array and 180 mJy $Hz^{-1/2}$ for the antenna-coupled KID array. Both numbers refer to a single typical pixel and at 1 Hz. In terms of the optical NEP, with reasonable assumptions on the optical transmission chain and the pixel geometry, we estimate an average 2.3×10^{-16} W $Hz^{-1/2}$ for the LEKID array and about 1.5×10^{-15} W $Hz^{-1/2}$ for the antenna-coupled array, both at 1 Hz. These values include a 50% factor which accounts for the impinging power reduction due to the polarizer. No further corrections have been applied to account for the detectors intrinsic optical efficiency. Millimeter-wave Vector Network Analyzer measurements performed at room temperature on the LEKID array indicate a good radiation coupling, with a peak absorption (central frequency) exceeding 80% (Roesch et al. 2010). Three-dimensional EM

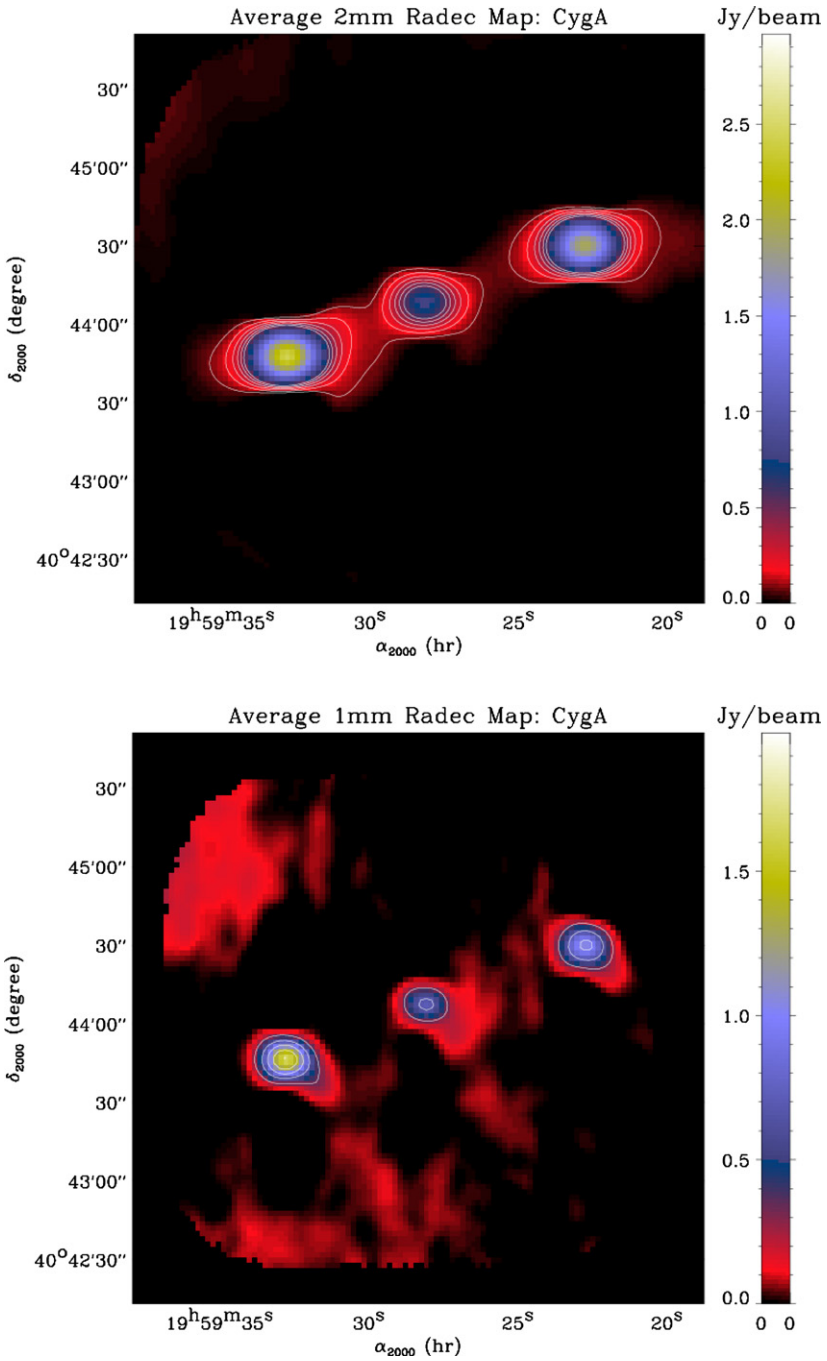

Figure 10. Maps at 2 and 1.4 mm of the radio source Cygnus A and its two radio lobes. All the three sources are detected at both wavelengths. Contours are at levels of 0.088 Jy beam^{-1} (resp. 0.332 Jy beam^{-1}) and multiples at 1.4 (resp. 2 mm). A Gaussian smoothing of 8 arcsec has been applied to the maps.
(A color version of this figure is available in the online journal.)

simulations suggest about 65% for the antenna-coupled array optical absorption. The estimated NEP is, for both arrays, in good agreement with the preliminary values obtained using the sky simulator.

6. CONCLUSIONS AND PERSPECTIVES

Work on the NIKA instrument commenced in 2008 November. At that time, no millimeter-wave LEKID had been designed and fabricated while substantial research on millimeter-wave antenna-coupled KID designs had been conducted (Schlaerth et al. 2008). In only two years, NIKA has developed rapidly and the 150 GHz LEKID array sensitivity is now comparable to the existing IRAM instrument MAMBO2 at Pico Veleta. While the sensitivity of the 220 GHz antenna-coupled array did not attain the target performance during this run, no significant barrier exists toward a substantial improvement in the near future.

For both arrays, further investigation is needed to achieve optimal photon-noise limited performance. Currently, a number of avenues are being pursued in order to achieve this goal.

1. New single-pixel geometries are being designed which promise to reduce pixel cross-talk, minimize detection volume, and absorb both polarizations.

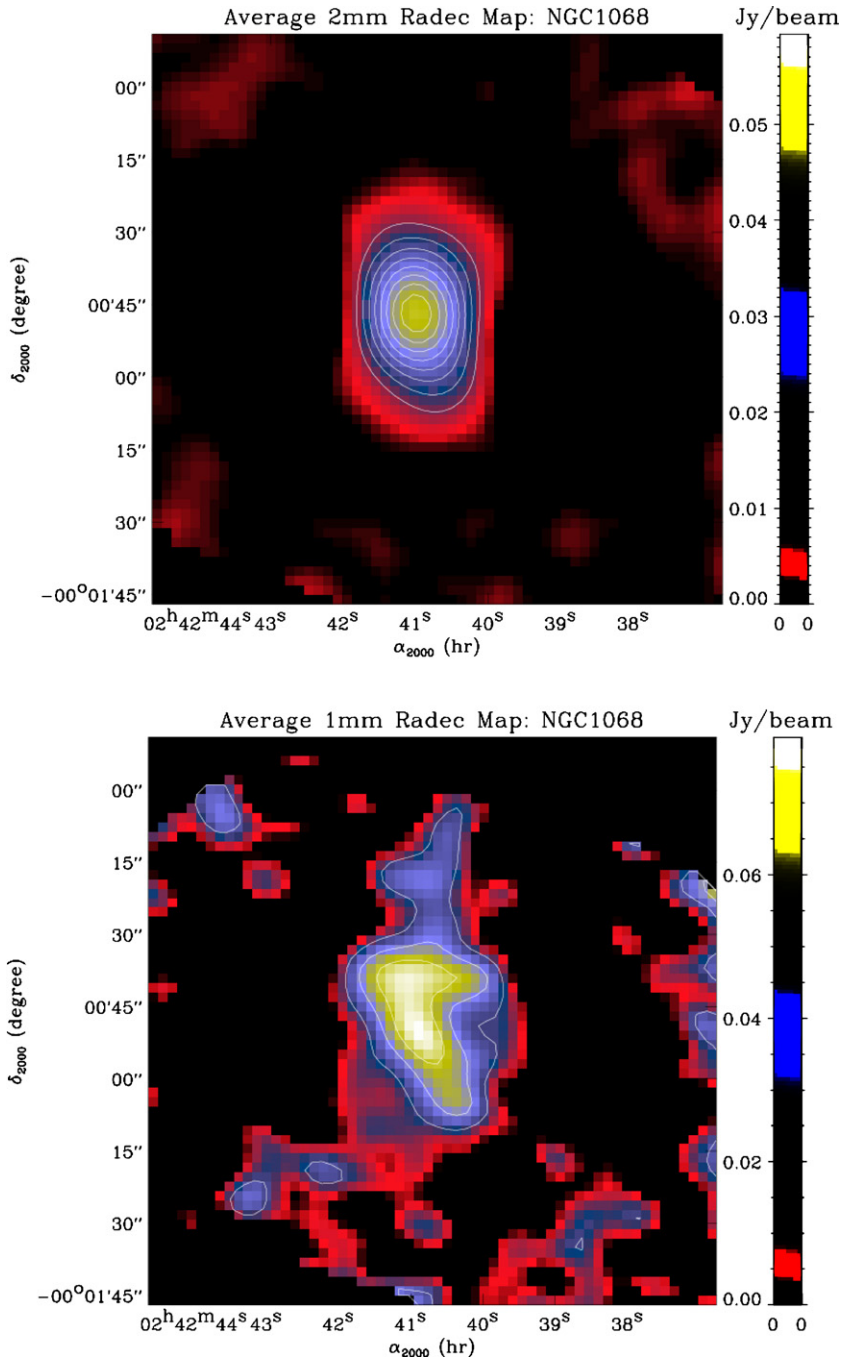

Figure 11. NIKA maps of NGC1068 galaxy at 2 and 1.4 mm wavelengths. The pixel size is 2 arcsec. The maps have been smoothed with an 8 arcsec Gaussian. Contours are at the levels of 9.2 mJy beam^{-1} × (2, 3, . . . , 7) for the 2 mm channel and 21, 42, 63 mJy beam^{-1} for the 1.4 mm channel.
(A color version of this figure is available in the online journal.)

2. Promising materials such as TiN are being characterized which may drastically improve the quantum efficiency of the detectors (Leduc et al. 2010).
3. The readout procedure continues to be optimized. A poor photometric precision, of the order of 30%, was obtained during this run. Development of new models of the underlying superconducting physics is necessary to better understand the pixel response to incident radiation. A new offline procedure is under development to include the $\partial\phi/\partial f$ nonlinearity and thus improve the photometric accuracy. Also, leveraging experience acquired during previous bolometer array development, we are implementing a modulation-based readout procedure that should simplify and improve the photometry by providing the frequency response of every pixel in real time.
4. New readout electronics are being developed to further increase the multiplexing (MUX) factor of each readout cable. The current instrument allows 112 pixels to be read out simultaneously in 233 MHz of bandwidth. Compared with the first version of NIKA, this is a six-fold improvement in the MUX factor. While a significant increase, digital electronics are readily available that can further improve the MUX factor by more than an order of magnitude. In order to harness this technology, we are developing a NIKA-dedicated readout system called NIKEL (NIKa ELectronics). A first generation NIKEL prototype, unused

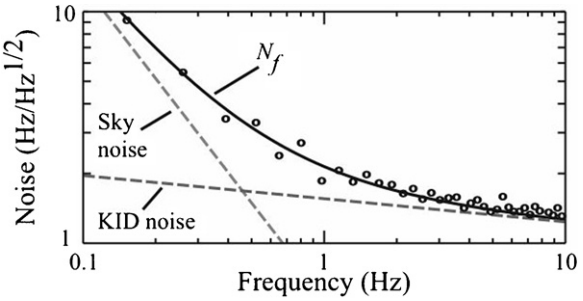

Figure 12. Frequency noise spectrum taken during a typical on-the-fly scan over the G34.3 galactic source. A fit of the function in Equation (4) yields the contribution to the noise due to low-frequency fluctuations from the source and sky ($\alpha = -1.35$) and the contribution at higher frequencies from the KIDs and the electronics ($\beta = -0.15$).

in the current measurement, achieved 128 channels over a bandwidth of 125 MHz (Bourrion et al. 2011). The next generation NIKEL system is under development and will achieve more than 256 channels over ∼400–500 MHz of bandwidth, using 12 bit analog-to-digital converters.

5. While greater magnetic shielding was utilized for the second generation NIKA system, magnetic field effects still limited the system performance. In particular, Earth's magnetic field was evident when changing the telescope azimuth angle. Changes in elevations did not strongly affect the current detectors, but potentially limit the performance of higher sensitivity instruments. Using a large current-carrying coil of wire, it is now possible to mimic the observed effects due to Earth's field in the laboratory. This new testing capability will allow a much more robust magnetic screening to be implemented and tested before installation at the telescope.
6. Improved baffling and filters are being designed to continue reducing spurious radiation. Compared with the previous NIKA run, the current instrument reduced the stray light by more than a factor of two but stray light continues to degrade the detector performance.
7. NIKA will move to a cryogen-free system. While not affecting the system sensitivity, the use of a standard dilution cryostat is a practical limitation prohibiting long-term installation of NIKA at the Pico Veleta telescope. The new cryogen-free cryostat has already been fabricated and is currently undergoing testing.

The current version of NIKA demonstrates the potential for KIDs to operate in large, ground-based millimeter-wave instruments. The NIKA project goal is to be a 6 arcmin field-of-view, dual-band resident instrument at the 30 m Pico Veleta telescope. In order to preserve the telescope intrinsic angular resolution, a Nyquist sampling of the focal plane is targeted ($0.50F\lambda$). This requires ∼1500 pixels at 150 GHz and ∼3000 pixels at 220 GHz. As an intermediate step to achieving this specification, NIKA will be upgraded to a cryogen-free, dual-band instrument covering a field of view of about 3 arcmin. Assuming the present $\approx 0.75F\lambda$ sampling, a 224 pixel array working at 150 GHz and a 489 pixel array at 220 GHz are required. Assuming a MUX factor of 256, only three cold amplifiers and six coaxial cables are necessary. A forthcoming measurement, implementing these system improvements is planned for the near future.

We thank Santiago Navarro, Juan Peñalves, Frédéric Damour, Carsten Kramer, David John, Juan Luis Santarén, Denise Riquelme, Salvador Sanchez, Hans Ungerechts, Robert Zylka, and all the IRAM staff for the excellent technical support during the run. We also acknowledge the technical staff at Institut Néel that have built the NIKA cryostat and participated in the electronics development, in particular Henri Rodenas, Gregory Garde, Anne Gerardin, Julien Minet and in general the Cryogenics and Electronics Groups. This work was supported in part by grant ANR-09-JCJC-0021-01 of the French National Research Agency, the Nanosciences Foundation of Grenoble and Région Rhône-Alpes (program CIBLE 2009). Part of the travel funds for the run have been provided by the French Ministère des Affaires étrangères et européennes (PHC Alliance 2010). This work is supported, in the UK, by STFC. This research, and in particular A. Baryshev, was supported ERC starting Researcher Grant ERC-2009-StG 240602 TFPA. Akira Endo is financially supported by NWO (VENI grant 639.041.023) and the Netherlands Research School for Astronomy (NOVA). We acknowledge the crucial contributions of Ben Mazin (UCSB), Bruno Serfass (Berkeley), and the OSR (Open Source Readout for MKIDs) Collaboration to the NIKA 2010 electronics.

Facility: IRAM:30m

REFERENCES

Barends, R., Vercruyssen, N., Endo, A., de Visser, P. J., Zijlstra, T., Klapwijk, T. M., & Baselmans, J. J. A. 2010, Appl. Phys. Lett., 97, 033507
Benoit, A., et al. 2008, Proc. SPIE, 7020, 702009-9
Bideaud, A. 2010, PhD thesis (in French), Université Joseph Fourier, Grenoble, France
Birkinshaw, M. 1999, Phys. Rep., 310, 97
Blain, A. W., Smail, I., Ivison, R.-J., Kneib, J.-P., & Frayer, D. T. 2002, Phys. Rep., 369, 111
Bourrion, O., et al. 2011, J. Instr., submitted (arXiv:1102.1314)
Day, P. K., LeDuc, H. G., Mazin, B. A., Vayonakis, A., & Zmuidzinas, J. 2003, Nature, 425, 817
Doyle, S., et al. 2009, in AIP Conf. Proc. 1185, 13th International Workshop On Low Temperature Detectors, ed. B. Young, B. Cabrera, & A. Miller (Melville, NY: AIP), 156
Duan, R., et al. 2010, Proc. SPIE, 7741, 77411V
Durand, T. 2007, PhD thesis, Université Joseph Fourier, Grenoble, France (in French)
Eales, S. A., Alexander, P., & Duncan, W. D. 1989, MNRAS, 240, 817
Gao, J. 2008, PhD thesis, California Institute of Technology, USA
Gao, J., Zmuidzinas, J., Mazin, B. A., LeDuc, H. G., & Day, P. K. 2007, Appl. Phys. Lett., 90, 102507
Hildebrand, R. H., et al. 1977, ApJ, 216, 698
Krips, M., Eckart, A., Neri, R., Schödel, R., Leon, S., Downes, D., García-Burillo, S., & Combes, F. 2006, A&A, 446, 113
Lagache, G., Puget, J.-L., & Dole, H. 2005, ARA&A, 43, 727
Leduc, H. G., et al. 2010, Appl. Phys. Lett., 97, 102509
Mazin, B. 2004, PhD thesis, California Institute of Technology, USA
Monfardini, A., et al. 2010, A&A, 521, A29
Parsons, A., et al. 2006, in Proc. Asilomar Conf. on Signals and Systems, 2031
Roesch, M., et al. 2010, Proc. SPIE, 7741, 77410N
Schlaerth, J., et al. 2008, J. Low Temp. Phys., 151, 684
Schwan, D., et al. 2010, arXiv:1008.0342v1
Swenson, L. J., Cruciani, A., Benoit, A., Roesch, M., Yung, C. S., Bideaud, A., & Monfardini, A. 2010, Appl. Phys. Lett., 96, 23
Swenson, L. J., et al. 2009, in AIP Conf. Proc. 1185, 13th International Workshop On Low Temperature Detectors, ed. B. Young, B. Cabrera, & A. Miller (Melville, NY: AIP), 84
Thronson, H., Walker, C. K., Walker, C. E., & Maloney, Ph. 1987, ApJ, 318, 645
Wright, M. C. H., & Birkinshaw, M. 2004, ApJ, 614, 115
Ward-Thompson, D., et al. 2007, Protostars and Planets V (Tucson, AZ: Univ. Arizona Press)
Yates, S. J. C., Baselmans, J. J. A., Baryshev, A. M., Klein, B., & Güsten, R. 2009, Appl. Phys. Lett., 95, 042504